Luca Imponenti
Mem. ASME
National Renewable Energy Laboratory,
15013 Denver West Parkway,
Golden, CO 80111;
Solar Dynamics LLC,
1105 W. 11th Court.,
Broomfield, CO 80020
e-mail: Luca.Imponenti@solardynllc.com

Ryan Shininger
Solar Dynamics LLC,
1105 W. 11th Court,
Broomfield, CO 80020
e-mail: ryan.shininger@solardynllc.com

Keith Gawlik
Solar Dynamics LLC,
1105 W. 11th Court,
Broomfield, CO 80020
e-mail: Keith.Gawlik@solardynllc.com

Hank Price
Solar Dynamics LLC,
1105 W. 11th Court,
Broomfield, CO 80020
e-mail: hank.price@solardynllc.com

Guangdong Zhu[1]
Mem. ASME
National Renewable Energy Laboratory,
15013 Denver West Parkway,
Golden, CO 80111
e-mail: guangdong.zhu@nrel.gov

Controllable Solar Flux Heating for Freeze Recovery in Molten Salt Parabolic Trough Collectors

In molten-salt parabolic trough plants, the melting process is particularly important for freeze recovery of salt that is solidified in a collector loop, should such an event occur. Currently impedance heating is expected for freeze recovery of the collector loops, but this method can be expensive. A lower-cost alternative is proposed to use controllable concentrated solar flux directly from the parabolic mirrors to thaw salt that is frozen in the collector. A computational fluid dynamics model was developed to explore the solidification and melting processes of molten salt in a parabolic trough receiver and to assess the viability of this concept. Results indicate that concentrated solar heating has the potential to melt frozen salt in 5.6 h, compared to that in 8.8 h for a 300 W m^{-1} impedance heating system. At the same time, controllable solar flux heating introduces nonuniform solar fluxes on the receiver surface, which can induce significant thermal stress on the receiver tube. A preliminary stress analysis indicates that the temperature difference across the receiver tube should be maintained below about 70 °C for heating up to 300 °C at internal pressures ≤10 bar. At these conditions, freeze recovery using solar flux heating will not significantly affect receiver lifetime. These results suggest that controllable solar flux heating could effectively supplement or replace impedance heating in the freeze recovery system. Incorporating this methodology in future parabolic trough concentrating solar power plants is an opportunity for capital and operational cost-savings.
[DOI: 10.1115/1.4047303]

Keywords: molten salt, parabolic trough, freeze protection & recovery

1 Introduction

Parabolic troughs are one of main concentrating solar power (CSP) technologies in the current market [1–3], as illustrated in Fig. 1(*a*). Total parabolic trough-installed capacity has reached about 6.3 GWe and dominates the global CSP market as of the end of 2018 [4]. Thermal energy storage (TES) can be coupled naturally with parabolic trough and other CSP technologies, enabling valuable dispatchability of CSP in the future grid with high penetration of non-flexible renewable energy [5]. The state-of-the-art TES adopts molten salt as the working media because of its low cost and high heat capacity. Many currently operating parabolic trough plants use an organic heat-transfer fluid (HTF) with maximum operating temperatures around 400 °C to transfer the heat from the solar field to the salt storage tanks [6–8]. This indirect approach for TES requires heat exchangers to move heat between the storage tanks and organic HTF, increasing the cost per kilowatt hour stored [7,8].

A direct approach currently being considered entails using the molten-salt storage media as the HTF in the solar field, significantly reducing the cost of TES [9,10]. This direct approach will also boost the solar field–operating temperature to increase the power-cycle efficiency and – combined with the cost reduction for TES – reduce the levelized cost of energy of the plant. Salt mixtures operate within a limited temperature range due to high freezing temperatures (90–220 °C) and relatively low stability limits (≤560 °C) [11,12]. The freezing temperatures being higher than ambient mean that there is a possibility for the salt to freeze in the solar field during its operational lifetime (25–30 years), and the plant must be designed to recover from such an occurrence [13,14]. A traditional approach for thawing the salt frozen in the collector loop is heat tracing in the header piping and using impedance heating in the receiver tubes [13,15]. Although this is a technically effective method, such a freeze protection system is estimated to cost 80 $ m^{-2}, adding up to 47% to the installed solar field cost for a large CSP plant [16,17]. A new approach using controllable solar flux heating is proposed to thaw salts for freeze recovery in direct molten-salt parabolic trough receivers. This method tailors the tracking of parabolic trough collectors to control the level of solar flux on the receiver with frozen salt during the day, so that the frozen salt can be melted without harming the receiver tube due to induced thermal stress.

The melting and solidification of multi-component salt mixtures is a complex phenomenon with many applications in the energy industry [11,18,19]. Common salt mixtures used for TES include solar salt and HITEC [11,12]. Neither of these nitrate salts is a eutectic composition, meaning the melting process occurs over a temperature range as opposed to a single melting temperature. The thermal properties and phase-change thermodynamics have a significant effect on heat transfer, and thus, on thermal stresses induced in the receiver tube [20,21]. However, the large-density

[1]Corresponding author.

Contributed by the Advanced Energy Systems Division of ASME for publication in the Journal of Energy Resources Technology. Manuscript received November 11, 2019; final manuscript received March 15, 2020; published online June 12, 2020. Assoc. Editor: Navid Goudarzi.

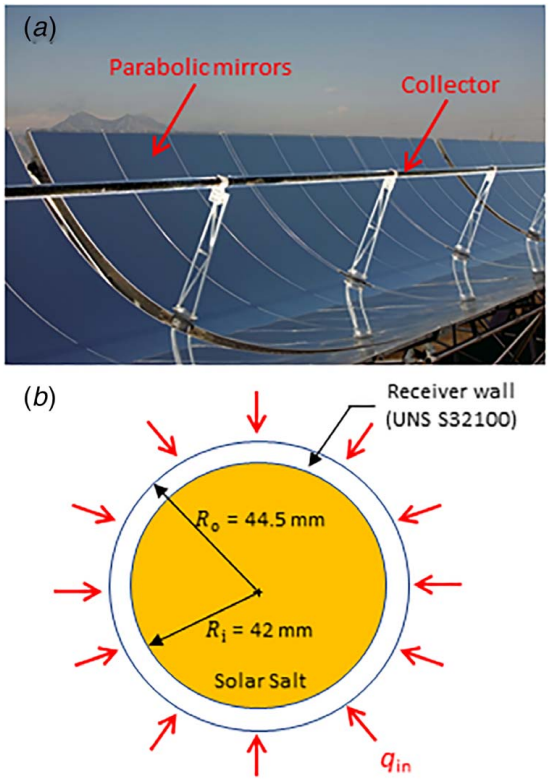

Fig. 1 (*a*) Photo of parabolic trough showing mirrors and collector [36], and (*b*) the domain modeled in ANSYS FLUENT consists of the receiver tube within the collector. The solar component of q_{in} varies circumferentially along the receiver wall, eliminating any planes of symmetry.

variations and phase change requires a computationally expensive model with three phases (frozen salt, molten salt, and void space) to capture all pertinent physics [22–24]. Initial modeling efforts rely on several simplifications to reduce the complexity of the thermal-fluid model, allowing the simulation of several different heating conditions for comparison.

This work investigates the melting of frozen solar salt in a receiver tube using controllable solar flux heating with comparison to the impedance heating method, exploring the potential technical and economic benefits of the proposed approach. Section 2 provides details of the geometry, governing equations, and boundary conditions for the computational fluid dynamics (CFD) model. Section 3 describes the methodology used to calculate thermal stresses in the receiver tube. Grid independence of the solution is demonstrated in Sec. 4. In Sec. 5, the computational model is verified by comparing with an analytical solution for the melting of a pure substance. Results of this modeling endeavor – including timescales for melting and allowable thermal stresses – are presented in Sec. 6. Finally, the concluding discussion can be found in Sec. 7.

2 Model Description

ANSYS FLUENT 18.2 is adopted to perform a two-dimensional (2D) model on a typical cross section of the receiver tube in a parabolic trough collector, as illustrated in Fig. 1(*a*). The 2D model solves equations for the conservation of momentum and energy considering laminar flow and melting of the two-phase salt mixture in the fluid domain. In the wall domain, the energy equation is also solved in 2D and coupled to the fluid domain. At the outer wall surface, the boundary heat flux can vary as a function of space and time. Due to the complexity of the problem being investigated, several assumptions help to make this modeling effort affordable: the salt is assumed to have constant density and to completely fill the receiver tube, thus neglecting density changes and subsequent formation of void spaces; species transport is neglected in the salt, and average properties are input to the model for the solar salt binary mixture, as opposed to a mixing law. The computational resources required to solve the problem are significantly reduced by considering the conduction limited heat transfer problem with a constant density salt. Furthermore, the constant density assumption excludes natural convection heat transfer resulting in conservative melt time estimates. This model is used to investigate several different flux profiles and gain understanding of trends in melt time and thermal stresses in the receiver tube. Once a flux profile is downselected, future modeling studies will investigate the effects of species transport and variations in density on the thawing and freezing process.

2.1 Geometry. An example of a parabolic trough collector and the 2D receiver geometry modeled in ANSYS FLUENT is illustrated in Fig. 1. The receiver tube is stainless steel 321, and the flow area is filled with Solar Salt. In a collector loop, the receiver tube will be enclosed in an evacuated glass casing; this casing is not modeled because the temperature profile of the glass is not a concern, and heat losses can be accurately quantified with an empirical expression for a similar receiver [25].

2.2 Governing Equations. The computational domain includes both the salt mixture and the receiver wall. In the fluid domain, a single-phase model includes both frozen and molten-salt states. The governing equations described in this section are adapted from the ANSYS Fluent Theory Guide [26]. An enthalpy-porosity technique is used for the phase-change region, where the solid/liquid interface is not tracked explicitly. Instead, the fraction of molten salt in each cell is tracked as an independent variable, i.e., the liquid fraction β. For each cell, β is calculated based on the cell temperature and salt phase diagram as shown in Eq. (1).

$$\begin{aligned} \beta &= 0 \quad \text{if} \quad T \le T_{\text{solidus}} \\ \beta &= 1 \quad \text{if} \quad T \ge T_{\text{liquidus}} \\ \beta &= \frac{T - T_{\text{solidus}}}{T_{\text{liquidus}} - T_{\text{solidus}}} \quad \text{if} \quad T_{\text{solidus}} < T < T_{\text{liquidus}} \end{aligned} \tag{1}$$

Cells where $0 < \beta < 1$ are referred to as the mushy zone; these cells are modeled as a porous medium where the porosity is related to the liquid fraction. For fully solid regions, the porosity and thus the velocity are zero. The single-phase formulation means that a single mass conservation expression is required, as written in Eq. (2). For all equations in the model description, density is considered an independent variable because eventually, the goal is relaxing the assumption of constant density

$$\frac{\partial \rho}{\partial t} + \nabla \cdot (\rho \boldsymbol{\nu}) = 0 \,. \tag{2}$$

Similarly, a single energy equation is written for the salt mixture in Eq. (3), including temperature-dependent thermal conductivity, γ, and enthalpy, H. To account for phase transition energetics, a latent heat term is included in H that is proportional to β and the heat of fusion Δh_f. The full expression for enthalpy is shown in Eq. (4)

$$\frac{\partial}{\partial t}(\rho H) + \nabla \cdot (\rho \boldsymbol{\nu} H) = \nabla \cdot (\gamma \nabla T) \tag{3}$$

$$H = h_{\text{ref}} + \int_{T_{\text{ref}}}^{T} c_p dT + \beta \Delta h_f \tag{4}$$

For conservation of momentum, shown in Eq. (5), the enthalpy-porosity model calls for an additional source term to account for the momentum sink in regions with where some solid exists.

$$\frac{\partial}{\partial t}(\rho \boldsymbol{\nu}) + \nabla \cdot (\rho \boldsymbol{\nu}\boldsymbol{\nu}) = -\nabla p + \nabla \cdot \left[\mu\left(\nabla \boldsymbol{\nu} + \nabla \boldsymbol{\nu}^T - \frac{2}{3}\nabla \cdot \boldsymbol{\nu} I\right)\right] + \rho \mathbf{g} + \frac{(1-\beta)^2}{(\beta^3 + \varepsilon)} A_{\text{mush}} \boldsymbol{\nu} \tag{5}$$

In the last term in Eq. (5), A_{mush} is the mushy zone set constant to 10^5 for all simulations discussed, and ε is a small number (0.001) to prevent dividing by zero.

The receiver tube wall is also meshed and modeled using ANSYS FLUENT. Due to the relatively slow heat, conduction dominated, transfer between the inner tube wall and enclosed salt, as well as the nonuniform boundary heat fluxes considered, both radial and circumferential conduction within the tube wall are important. In the receiver wall domain, the energy equation reduces to Eq. (6)

$$\rho_w c_{p,w} \frac{\partial T_w}{\partial t} = \nabla \Delta(\gamma_w \nabla T_w) \tag{6}$$

where the subscript w indicates a wall property. Accurately capturing the wall temperature profile is critical for thermal stress calculations.

These equations are solved using ANSYS FLUENT 18.2 with the SIMPLE pressure–velocity coupling. The spatial discretization schemes are as follows: least squares cell based for gradients, second order for pressure, and second-order upwind for momentum and energy. Stringent convergence criteria are required in solidification and melting problems, i.e., 10^{-5} for continuity and velocity residuals, and 10^{-8} for the energy equation [23].

2.3 Boundary Conditions. The boundary heat flux is a combination of concentrated solar heat, heat losses to the environment, and impedance heat depending on the simulation, as shown in Eq. (7). Solar heat concentrated using the parabolic mirrors varies spatially and temporally, eliminating any planes of symmetry. Although impedance heat is generally constant around the receiver tube, simulations with only impedance heating are solved using the same domain and mesh.

$$q_{\text{in}} = q_{\text{solar}} + q_{\text{imp}} - q_{\text{loss}} \tag{7}$$

$$q_{\text{loss}}(\text{W m}^{-1}) = \frac{2R_o}{0.07}(0.141 T_{^\circ\text{C}} + 6.48 \times 10^{-9} T_{^\circ\text{C}}^4) \tag{8}$$

The heat- loss equation used in this work is an empirical correlation determined from indoor testing of a similar receiver of smaller diameter [25]. Equation (8) is scaled by the receiver diameter (in m) to account for the different geometry. The expression has a fourth-order term attributed to radiation as well as a linear term attributed to convection. The cell temperature should be in Celsius for determining heat losses using Eq. (8), as indicated by the °C subscript. The equation for q_{loss} is also plotted in Fig. 2; at higher temperatures, the plot is dominated by radiation effects assuming vacuum conditions between the receiver tube and the glass casing [25,27]. This parameter has significant effects on simulation results for both heating and cooling of the receiver and should be chosen carefully based on the receiver geometry and ambient conditions. Using the expression for q_{loss}, it is trivial to calculate the minimum heat required to melt salt within the receiver, $q_{\text{melt}} = q_{\text{loss}}(T_{\text{solidus}})$. For the selected T_{solidus} and heat-loss equation, $q_{\text{melt}} = 74.8$ W m^{-1}, as seen in Fig. 2.

Inside the receiver tube, a no-slip condition is imposed at the inner wall boundary. Heat transfer at this inner wall boundary is inherently calculated by Fluent based on the properties and fluid dynamics in the salt domain.

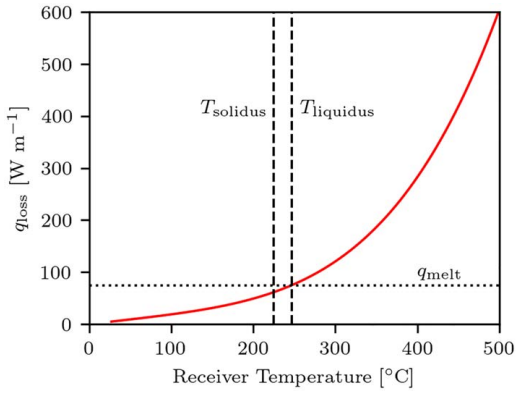

Fig. 2 Heat-loss equation used in receiver tube simulations. The vertical dashed lines indicate the solar salt phase change temperature region [28]. The horizontal dotted line is the minimum heat input to keep salt from solidifying assuming uniform heating.

2.4 Material Properties. The properties input to Fluent for the Solar Salt are described in Table 1. Species diffusion is neglected in this model, so properties are input as if the mixture were a single component. Significant literature exists on measuring properties of molten solar salt [12,28–30], whereas there are much less data available for the frozen state [31]. Most properties are assumed constant in the frozen state except for viscosity, μ, and heat conductivity, γ. Properties only documented for the pure components were averaged on a mass basis, including the enthalpy of fusion Δh_f and ρ. Since ρ is assumed constant, a single value must be selected; in this study, the solid-phase value for ρ is chosen to study the case with the most thermal mass. This approach should yield conservative estimates for the time required to melt salt within the receiver tube t_{melt}.

The receiver wall is made of stainless steel 321 (UNS S32100); properties of the wall material are detailed in Table 2. Properties required for the thermal stress analysis, described in the following section, are also included in Table 2.

Table 1 Properties of solar salt mixture input to ANSYS FLUENT model

Property	Value	Source
T_{solidus} (K)	498	[28]
T_{liquidus} (K)	520	[28]
Δh_{f} (J kg^{-1})	146,537	[29]
ρ (kg m^{-3})	2232	[30]
c_{p} (J kg^{-1} K^{-1})	1553	[12,30,37]
μ (kg m^{-1} s^{-1})	$7.551(10^{-2}) - 2.775(10^{-4})T + 3.488(10^{-7})T^2 - 1.474(10^{-10})T^3$	[12,30]
γ (W m^{-1} K^{-1})	$0.56415 - 1.55527(10^{-4})T$	[30]

Table 2 Properties of stainless steel 321 (UNS S32100) used to model the receiver wall

Property	Value	Source
ρ (kg m^{-3})	7,900	[38]
c_{p} (J kg^{-1} K^{-1})	500	[38]
γ (W m^{-1} K^{-1})	$10.41175 + 0.01525 \cdot T$	[38]
E (GPa)	193	[38]
α (K^{-1})	$17.0 \cdot 10^{-6}$	[38]
ν	0.27	[38]

3 Thermal Stress Calculation Approach

Once the temperature profile in the receiver wall is known from solving the CFD model described in Sec. 2, thermal stresses are approximated using a biharmonic approach for non-axisymmetrically heated tubes [21]. First, the average surface temperatures for the inner and outer wall boundaries, $\bar{T}_i$ and $\bar{T}_o$, are calculated as follows:

$$\bar{T}_i = \frac{1}{2\pi}\int_0^{2\pi} T d\theta \text{ for } r = R_i \tag{9}$$

$$\bar{T}_o = \frac{1}{2\pi}\int_0^{2\pi} T d\theta \text{ for } r = R_o \tag{10}$$

These temperatures are used in the definition of the circumferentially varying temperature fluctuation expression, T_θ referenced to the average outer surface temperature

$$T_\theta = T - (\bar{T}_i - \bar{T}_o)\frac{\ln R_o/r}{\ln R_o/R_i} - \bar{T}_o \tag{11}$$

$$T_\theta = \sum_{n=1}^{\infty}(A_n r^n + B_n r^{-1})\cos n\theta + (C_n r^n + D_n r^{-1})\sin n\theta \tag{12}$$

Referring to Eq. (6), a harmonic Fourier series exists with radial-dependent functions that can satisfy the energy equation in the wall domain; T_θ is represented by such an equation in Eq. (12). A least-squares fitting algorithm is used to fit values of T_θ calculated with Eq. (11) to the expression in Eq. (12), yielding the coefficients A_n, B_n, C_n, and D_n. The fitted parameters B_1 and D_1 are important for thermal stress calculations. Expressions for the radial and circumferential components of stress in a non-axisymmetrically heated cylinder are written in Eqs. (13) and (14), respectively

$$\sigma_r = K\frac{\alpha E}{2(1-\nu)}\left[-\ln\frac{R_o}{r} - \frac{R_i^2}{R_o^2 - R_i^2}\left(1 - \frac{R_o^2}{r^2}\right)\ln\frac{R_o}{R_i}\right] + K_\theta\frac{\alpha E}{2(1-\nu)}\left(1 - \frac{R_i^2}{r^2}\right)\left(1 - \frac{R_o^2}{r^2}\right) \tag{13}$$

$$\sigma_\theta = K\frac{\alpha E}{2(1-\nu)}\left[1 - \ln\frac{R_o}{r} - \frac{R_i^2}{R_o^2 - R_i^2}\left(1 + \frac{R_o^2}{r^2}\right)\ln\frac{R_o}{R_i}\right] + K_\theta\frac{\alpha E}{2(1-\nu)}\left(3 - \frac{R_i^2 + R_o^2}{r^2} - \frac{R_i^2 R_o^2}{r^4}\right) \tag{14}$$

where E is Young's modulus for the receiver wall, α is the linear coefficient of thermal expansion, and υ is Poisson's ratio. The coefficients K in front of each term are defined in Eqs. (15) and (16) and represent contributions from $n = 0$ and 1, respectively:

$$K = \frac{\bar{T}_i - \bar{T}_o}{\ln R_o/R_i} \tag{15}$$

$$K_\theta = \frac{r}{R_i^2 + R_o^2}(B_1 \sin\theta + D_1 \cos\theta) \tag{16}$$

The shear component of thermal stress is calculated with Eqs. (17) and (18)

$$\sigma_{r\theta} = K_\tau\frac{\alpha E}{2(1-\nu)}\left(1 - \frac{R_i^2}{r^2}\right)\left(1 - \frac{R_o^2}{r^2}\right) \tag{17}$$

$$K_\tau = \frac{r}{R_i^2 + R_o^2}(B_1 \sin\theta - D_1 \cos\theta) \tag{18}$$

To estimate the axial component of shear stress from this 2D geometry, an assumption regarding the constraints of the receiver tube must be made. A commonly used reference case is the plane strain assumption, where the ends of the receiver tube are constrained from moving in the axial direction; a more appropriate assumption is that of net zero axial force in the receiver tube, referred to as a generalized plane strain state. Manipulating expressions of Hooke's law and assuming external mechanical loads are zero, Logie et al. (2018) derived an expression for axial stress, σ_x, assuming generalized plane strain, as shown in Eq. (19)

$$\sigma_x = K\frac{\alpha E}{2(1-\nu)}\left[1 - 2\ln\frac{R_o}{r} - \frac{2R_i^2}{R_o^2 - R_i^2}\ln\frac{R_o}{R_i}\right] + K_\theta\frac{\alpha E\upsilon}{(1-\nu)}\left(2 - \frac{R_i^2 + R_o^2}{r^2}\right) - \alpha E T_\theta \tag{19}$$

Once all the components of stress are calculated, the effective von Mises stress in the receiver tube is determined using Eq. (22). The von Mises stress is considered an appropriate value to compare with maximum allowable stresses in the receiver tube to understand viable operating conditions.

$$\sigma_{VM} = \sqrt{\frac{1}{2}[(\sigma_r - \sigma_\theta)^2 + (\sigma_\theta - \sigma_z)^2 + (\sigma_z - \sigma_r)^2] + 3\sigma_{r\theta}} \tag{20}$$

In addition to thermal effects, internal pressure can also contribute to stresses in the receiver tube. During normal operation, the glass casing enclosing the receiver tube is under vacuum to limit convection cooling effects; with this setup, all flow pressure within the tube contributes to the overall stress state [21]. For a generalized plane strain state, the stress due to internal pressure can be calculated as follows:

$$\sigma_r = \frac{pR_i^2}{R_o^2 - R_i^2}\left(1 - \frac{R_o^2}{r^2}\right) \tag{21}$$

$$\sigma_\theta = \frac{pR_i^2}{R_o^2 - R_i^2}\left(1 + \frac{R_o^2}{r^2}\right) \tag{22}$$

$$\sigma_x = \frac{pR_i^2}{R_o^2 - R_i^2} \tag{23}$$

where p indicates the internal pressure relative to the outside of the tube. During normal operation, p will be very similar to the absolute pressure and could be significant depending on the pressure drop through the collector loop.

4 Grid Independence

The receiver tube and enclosed fluid are discretized using a conformal mesh of triangular and quadrilateral elements. The two parameters considered for mesh independence are the time required to completely melt the salt, t_{melt}, and the maximum von Mises stress recorded in the receiver wall during the simulation, $\sigma_{VM,max}$. Both parameters are important to ensure that the mesh is refined in both the wall and fluid domains. The mesh independence simulation used pure solar heating at the outer boundary ($q_{imp} = 0$), and results for various mesh sizes are plotted in Fig. 3. In Fig. 3(*a*), t_{melt} is plotted as a function of mesh size in the fluid domain. This parameter remains relatively constant for different grid sizes, suggesting that the coarsest mesh tested (1 mm) could be appropriate in the fluid domain. In Fig. 3(*b*), $\sigma_{VM,max}$ is plotted as a function of mesh size in the wall domain. The results indicate that a much finer mesh is required for grid-independent results in the wall compared with the fluid domain.

The grid independence study plotted in Fig. 3 suggests that the wall domain requires a significantly smaller element; however, meshing the entire domain with a small enough grid size for accurate thermal stress calculations significantly increases the computational expense of the model. To achieve grid-independent results for

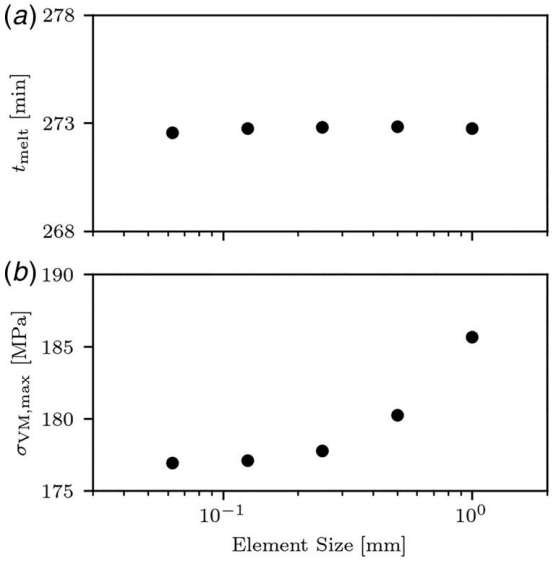

Fig. 3 Results of the mesh independence study for both wall and fluid domains: (*a*) time required to completely melt salt and (*b*) maximum von Mises stress for various mesh sizes

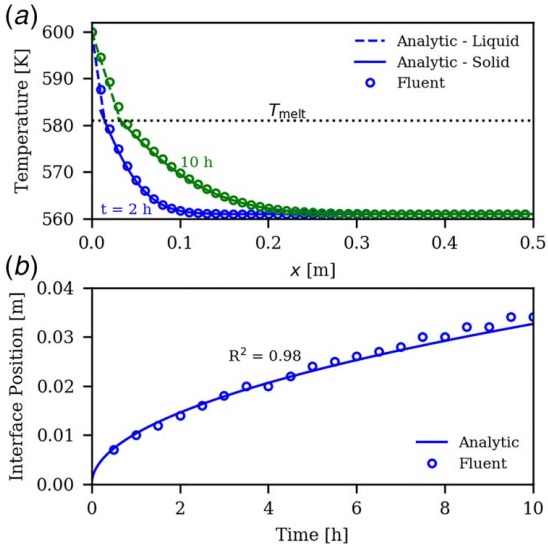

Fig. 4 (*a*) Temperature profiles for solid and liquid phases at selected time-steps, and (*b*) the transient location of the solid/liquid interface for the two-phase Stefan problem. The analytical solution is compared to ANSYS FLUENT model results.

both t_{melt} and $\sigma_{VM,max}$, the wall and fluid domains are meshed with different element sizes. The mesh remains conformal such that the nodes within the fluid domain match the wall domain nodes at the inner wall interface and grow toward the center of the receiver tube. The fluid domain mesh size was not reduced past 0.5 mm; in Fig. 3(*b*), using a finer mesh required for grid-independent results, the fluid domain mesh size remains fixed at 0.5 mm. The selected mesh has elements of 0.125 mm in the wall domain and 0.5 mm in the fluid domain for a total of 74,722 nodes.

5 Model Verification

The model is verified by comparing with the analytical solution of the two-phase Stefan problem solved on a semi-infinite domain in 1D, also known as the Neumann solution [32]. The semi-infinite domain is approximated in Fluent as a long rectangle, and the appropriate independent variables are sampled along the centerline for comparison. The Neumann solution yields the location of the solid/liquid interface and the temperature profile in both solid and liquid regions for a pure substance that undergoes a phase change. The fluid is initially frozen at a given temperature below the melting temperature T_{melt}. A constant temperature boundary condition is imposed at $x = 0$; this provides heat to melt the initially frozen fluid. For this case, the domain is initialized at 561 K and the wall is set to 600 K; the fluid considered is pure $NaNO_3$ with $T_{melt} = 581$ K.

Results for the benchmark case are shown in Fig. 4. The numerical simulation does an excellent job of capturing both the temperature profile plotted as in Fig. 4(*a*) and the location of the solid/liquid interface as shown in Fig. 4(*b*). In Fig. 4(*a*), the transition between liquid and solid phases is clearly visible where each temperature profile intersects the dotted line indicating T_{melt}. This simple benchmark case serves as verification of the solidification and melting module adopted for this work.

6 Results and Discussion

Using the CFD model described in Sec. 2 and thermal stress model in Sec. 3, several solar heat flux profiles are used to simulate the melting of solar salt within the receiver tube. Results for controlled solar flux heating are compared with those of currently used impedance heating systems, and the possibility of hybrid systems is explored.

6.1 Cost Analysis. Before looking at model results, the economics motivating the work is analyzed. The freeze protection system for a molten-salt parabolic trough plant involves feeder and header piping as well as the solar field. Insulated and stationary sections of piping will be heat traced, while impedance heating is expected for components of the solar field including collectors and interconnects. The estimated capital cost for freeze protection, including just the impedance heating system, is compared with the installed solar field cost in Table 3. The freeze protection system can add up to 47% to the installed solar field cost for a 100 MWe CSP plant [17]. The impedance heating system accounts for 67.5% of the cost for freeze protection. This work is focused on reducing the cost of the impedance heating system, taking advantage of the negligible capital cost required for controllable solar flux heating of the collectors. Reducing the cost of the impedance heating system by 50% would decrease total installed cost for the solar field and freeze the protection system from 220 to 193 \$ m^{-2}.

6.2 Impedance Heating. Salt frozen in the receiver tube can be melted via impedance heating of the tube itself or by using concentrated solar heat from the parabolic mirrors. Impedance heating is modeled as a uniform heat flux at the outer wall surface. The goal of this study is to assess the feasibility of using mirrors to thaw salt frozen in the receiver tube and also to understand what benefits this method of heating can offer over impedance heating in terms of cost and melting time. All melting simulations assume a uniform initial

Table 3 Estimated costs for relevant components of molten salt parabolic trough plants

Component	Cost (\$ m^{-2})	Source
Solar field	170	[17]
Freeze protection system	80	[16]
Impedance heating system	55	[16]

Note: The impedance heating system cost is also included as part of the freeze protection system cost.

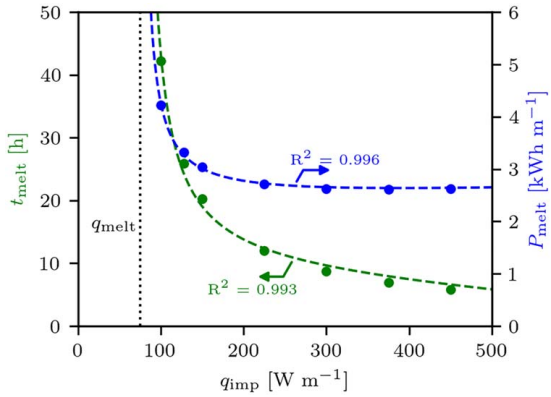

Fig. 5 Time and energy required to melt solar salt in receiver tube for different levels of impedance heating; simulation data are plotted with symbols and the dotted lines indicate curve fits

temperature of 10 °C (283 K) for both the salt and the receiver tube. This initial condition is a worst-case scenario assuming enough time has passed for thermal equilibration with the environment.

Impedance heating systems used in operational parabolic trough plants generally provide between 100 and 250 W m^{-1} spread uniformly around the receiver tube [13]. Results for melting simulations with pure impedance heating ($q_{solar} = 0$), including the time and energy required to completely melt the salt mixture (t_{melt} and P_{melt}), are summarized in Fig. 5. Note that these results are heavily dependent on the selected heat-loss equation, as plotted in Fig. 2. In this case, $q_{melt} = 74.8$ W m^{-1}; as discussed in Sec. 2.3, this value becomes a vertical asymptote in Fig. 5 because any lower heat inputs will not completely melt the salt mixture. As q_{imp} is increased from q_{melt}, the time and energy required to melt decrease sharply. t_{melt} continues to decrease in an exponential fashion as the heat input is increased; however, P_{melt} is relatively constant for $q_{imp} > 200$ W m^{-1}, reaching a minimum value of 2.64 kWh m^{-1} at $q_{imp} = 395$ W m^{-1}. For these higher impedance heating levels, a slightly faster t_{melt} does not compensate for the extra heat flux input to the receiver tube, resulting in a relatively constant P_{melt}.

The plots in Fig. 5 are plotted with fitted lines determined through a least-squares fitting algorithm. As discussed in the previous paragraph, the parameter q_{melt}, determined from the heat-loss equation, is of significant importance to the results plotted in Fig. 5. Mathematically, a vertical asymptote is represented by a term in the denominator, suggesting that the results for impedance heating simulations may be represented by a rational expression. For both t_{melt} and P_{melt}, excellent fits with $R^2 > 0.99$ were achieved with the second-order rational expression shown below

$$P_{melt} = \frac{a_2 q_{imp}^2 + a_1 q_{imp} + a_0}{q_{imp} - q_{melt}} \tag{24}$$

where a_0, a_1, and a_2 are fitting parameters, and q_{melt} is determined using the selected heat-loss equation.

6.3 Controllable Solar Flux Heating. Melting salt with controllable solar flux heating could be a low-cost alternative to impedance heating in the event of a freeze. Controllable solar flux heating takes advantage of the parabolic trough mirrors to concentrate solar radiation onto the receiver tube, thus providing heat for thawing. Generally, the parabolic mirrors are oriented north–south and track the sun from east to west throughout the day. During normal plant operation, the mirrors focus on the receiver tube to heat solar salt from 300 deg to 550 °C. Due to the lower receiver temperatures and inefficient heat transfer to the stagnant salt during freeze recovery, holding the mirrors on-focus results in high thermal gradients across the receiver. For this reason, the solar heating flux profile, q_{solar}, must be adjusted to prevent receiver failure.

Two examples of the spatially varying solar heat flux boundary condition are plotted in Fig. 6(*a*). In this manuscript, the bottom of the receiver ($\theta = 180$ deg) refers to the side closest to the parabolic mirrors. These are the two extreme conditions with the mirrors on-focus (high heat input) and the mirrors off-sun (low heat input). For the case when the mirrors are off-sun, the plotted values assume 1 sun (1000 W m^{-2}) at 0-deg incidence angle irradiating the top of the receiver. This heat flux is also included in calculations for the on-focus profile as seen by the matching values for $\theta < 45$ deg and >315 deg; however, in the on-sun case, this heat input is small compared to the concentrated heat from the mirrors. When the mirrors are on-focus, the bottom of the receiver tube heats very rapidly compared to the top, resulting in large temperature gradients and thermal stresses. The low conductivity of the salt mixture relative to the wall material does not allow heat to dissipate from the receiver tube into the salt before reaching critical stress levels. To mitigate excessive heating, the mirrors are cycled between on-focus and off-sun positions, resulting in the spatially averaged transient flux profile shown in Fig. 6(*b*). Different flux profiles are achieved by controlling how long the mirrors are held on-focus, t_{on}, how long the mirrors are held off-sun, t_{off}, and the mirror tracking speed to move between these two positions, $\dot{\theta}$.

Simulation results for several different solar heating flux profiles are detailed in Table 4. Flux profiles 13–15 are reference cases where the mirrors jump between on-focus and off-sun positions;

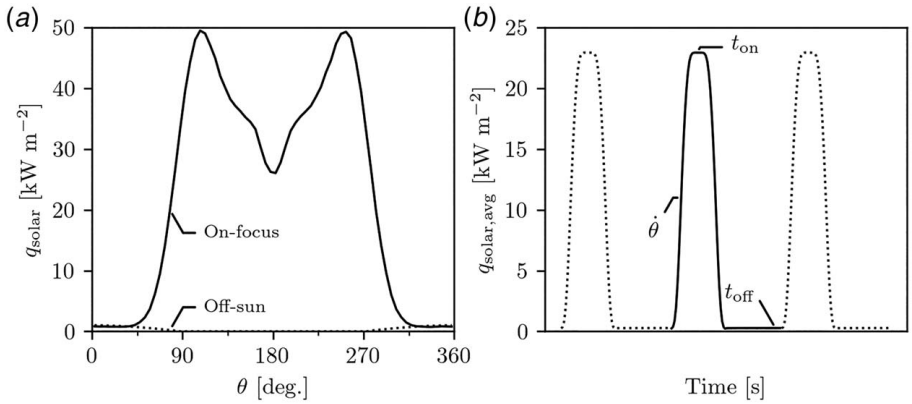

Fig. 6 (*a*) Heat flux profile at the outer receiver wall when mirrors are on-focus and off-sun, where 0 deg is the top of the receiver. (*b*) Typical transient flux profile input for mirror heating simulations; each point is the spatially averaged flux profile at any given time. By varying t_{on}, t_{off}, and $\dot{\theta}$, several different flux profiles are modeled

Table 4 Summary of results for thawing of frozen salt in the receiver tube from an initial temperature of 10 °C using only controllable solar flux heating

Flux profile ID	$\dot{\theta}$ (deg/s)	t_{on} (s)	t_{off} (s)	t_{cycle} (s)	$\bar{q}$ (W m^{-1})	t_{melt} (min)	$\Delta T_{w,max}$ (K)
1	0.3	5	210	451.3	401.15	389.9	61.17
2	0.3	5	120	271.3	608.44	274.6	95.35
3	0.3	10	210	461.3	531.75	306.3	88.27
4	0.3	3	120	267.3	521.39	316.4	78.04
5	0.3	1	120	263.3	431.70	379.3	60.20
6	0.1	5	210	494.0	688.55	250.4	132.42
7	0.1	1	210	486.0	594.10	285.0	114.22
8	0.1	1	300	666.0	457.50	359.6	91.27
9	0.5	5	210	442.8	337.03	472.3	41.78
10	0.5	5	120	262.8	507.13	320.9	72.10
11	0.5	10	210	452.8	471.51	339.9	73.57
12	0.5	3	120	258.8	415.64	387.7	53.18
13	∞	5	210	215.0	236.07	633.8	23.76
14	∞	5	120	125.0	342.18	426.5	40.92
15	∞	5	60	65.0	576.18	262.7	82.28

these simulations represent the theoretical limit where the mirrors track infinitely fast. Results suggest that there are multiple combinations of t_{on}, t_{off}, and $\dot{\theta}$ that will result in a similar $\Delta T_{w,max}$; in these cases, faster $\dot{\theta}$ appears to melt the salt quicker. For slower values of $\dot{\theta}$, a shorter t_{on} and longer t_{off} are required to allow the heat to dissipate and maintain reasonable receiver temperatures gradients. As $\dot{\theta}$ is increased, it is possible to decrease t_{off} while maintaining similar temperature differences, resulting in significantly faster cycle times.

Table 4 includes the average heat input per unit length, $\bar{q}$, calculated for each solar heating flux profile. $\bar{q}$ is the average function value as shown in Eq. (25); this parameter depends on the three control variables $\dot{\theta}$, t_{off}, and t_{on}. The averaged heat input during controllable solar flux heating results in a value easily comparable with impedance heating system power levels. Impedance heating systems provide uniform heat, so q_{imp} is not included in the circumferential integral and $\bar{q} = q_{imp}$ for cases with only constant impedance heating.

$$\bar{q} = \frac{1}{t_{cycle}} \int_0^{t_{cycle}} \left(q_{imp} + R_o \int_0^{2\pi} q_{solar} \right) \tag{25}$$

Results for solar heating are compared with the previously discussed impedance heating results in Fig. 7. The combined results of impedance and solar heating show similar trends for both heating methods, allowing for a single fit on all the simulation data using Eq. (24). With the added mirror heating simulation data points, the minimum melt energy is 2.59 kWh m^{-1} at 349 W m^{-1}, which is similar to results reported from pure impedance heating data points (2.64 kWh m^{-1} at 395 W m^{-1}) in terms of energy; but $\bar{q}$ to achieve this minimum energy is lowered significantly. With the added data points, a more distinct minimum followed by a linear increase is observed for P_{melt}, compared to impedance heating simulations where P_{melt} appeared to plateau after the minimum point. For P_{melt}, the added data points result in a slightly worse fit with the rational expression (R^2 lowered from 0.995 to 0.984), which appears to be caused by the variance in the solar heating data. For t_{melt}, Eq. (24) does a good job of capturing trends in the data for $\bar{q} \leq 600$ W m^{-1}, and at higher heat inputs, the fitted curve decreases linearly as opposed to the more asymptotic behavior observed in simulations.

The results plotted in Fig. 7 show that faster melt times were achieved with controllable solar flux heating compared to impedance heating. Much higher heat inputs are possible using the parabolic mirrors due to cost and mechanical constraints on pure impedance heating systems, which limit these systems to about 300 W m^{-1} [13]. The higher heat inputs possible with solar heating results in significantly faster t_{melt} compared to impedance systems; however, heating with mirrors also results in much higher thermal stresses, as shown by the wall temperature differences plotted in Fig. 8. For comparison, results for a 300 W m^{-1} impedance system indicate $t_{melt} = 8.8$ h with $\Delta T_{w,max} = 0.1$ °C, whereas flux profile 1 ($\bar{q} \approx 400$ W m^{-1}) results in $t_{melt} = 6.5$ h with $\Delta T_{w,max} = 61.2$ °C. The impedance heating system provides low levels of uniform heat resulting in low temperature gradients across the wall and slow t_{melt}. The concentrated solar heat is nonuniform, with high peak values as shown in Fig. 6(*a*), resulting in faster melting times with large temperature gradients. For these reasons, it is very important to monitor the temperature difference across the receiver wall, ΔT_w, during solar flux heating.

The maximum temperature difference across the receiver wall, $\Delta T_{w,max}$, observed during melting simulations with solar heating is plotted in Fig. 8. Results suggest that $\Delta T_{w,max}$ varies significantly with the mirror tracking speed, $\dot{\theta}$, as well as $\bar{q}$. For each value of $\dot{\theta}$, $\Delta T_{w,max}$ increases linearly as a function of $\bar{q}$. In some cases, significant differences in $\Delta T_{w,max}$ are evident comparing simulations with similar $\bar{q}$, e.g., flux profiles 8 and 11 with a 3% difference in $\bar{q}$ compared to a 19% change in $\Delta T_{w,max}$. In these cases, lower temperature differences are observed for flux profiles with faster $\dot{\theta}$. The reference cases show the limit of infinitely fast $\dot{\theta}$ such that mirrors jump from on-focus and off-sun positions; these simulations indicate the minimum possible $\Delta T_{w,max}$ for a given $\bar{q}$. Results at different mirror tracking speeds suggest that there is no benefit in moving the mirrors faster than 0.5 deg s^{-1}. For $\dot{\theta} \geq 0.5$ deg s^{-1}, the heat input during mirror tracking is minimal and $\Delta T_{w,max}$ can be well described as a function of $\bar{q}$ only. A more comprehensive thermal stress analysis on the wall temperature profiles is performed in Sec. 6.4 to understand which values of $\Delta T_{w,max}$ can be supported

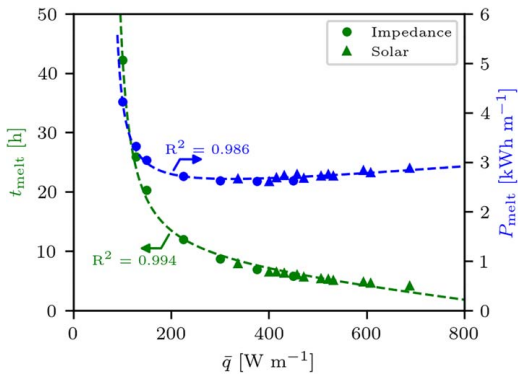

Fig. 7 Time and energy required to melt solar salt in receiver tube for simulations with pure impedance heating (circles) and mirror heating (triangles). Results for mirror heating simulations appear to follow similar trends as impedance heating

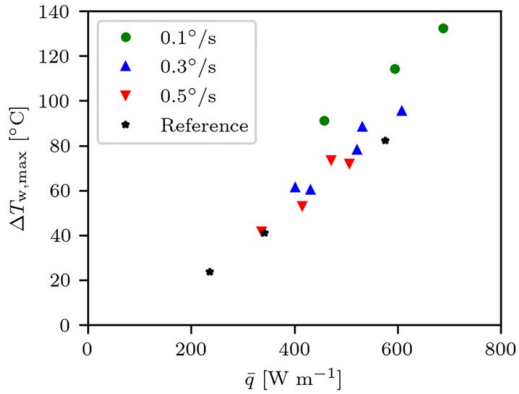

Fig. 8 Maximum wall temperature difference observed during heating as a function of average mirror heat input organized based on mirror tracking speed

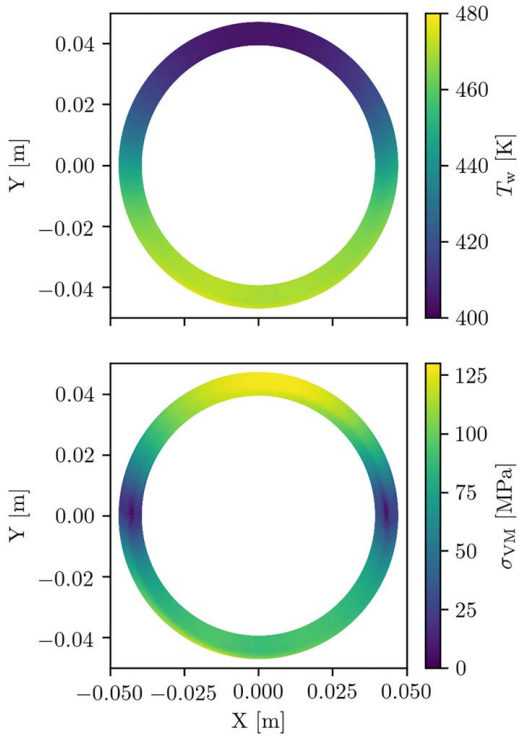

Fig. 9 Contour plots showing temperature (left) and von Mises stress at 1 bar (right) for flux profile 10 at a high stress point during the melting simulation

by the receiver tube. If possible, it is desirable to melt using solar heat and save on costs associated with impedance heating.

6.4 Thermal Stress Analysis. The thermal stresses are calculated based on the temperature profile output from the ANSYS FLUENT simulations using an analytical solution method [21], described in Sec. 2. The 2D temperature profile is used to calculate radial and circumferential components of stress, while the axial component is determined by manipulating Hooke's law assuming a generalized plane strain state. Each component of stress contributes to the effective von Mises stress, σ_{VM}, at any given location. A typical temperature profile and the resulting von Mises stress are plotted in Fig. 9; these results represent the largest recorded temperature difference for flux profile 2 a pressure of 1 bar. The temperature profile shown in Fig. 9(*a*) is representative of a typical profile at a high stress point when the receiver tube is heated purely with q_{solar}. Solar heat is focused toward the bottom part of the receiver with the mirrors before allowing time for heat to dissipate, thus maintaining a reasonable temperature gradient across the tube. This heating method results in large circumferential temperature gradients around the receiver tube, but relatively low gradients in the radial direction. Such a temperature profile results in the effective von Mises stress distribution shown in Fig. 9(*b*). The highest effective stress levels are at the top and bottom of the receiver, toward the outer radius.

The individual components of stress at 1 bar for flux profile 2 are also plotted in Fig. 10. The axial and circumferential components of stress, σ_x and σ_r, dominate the von Mises stress state. The radial and shear components, σ_r and $\sigma_{r\theta}$, are orders of magnitude lower than σ_x and σ_θ. All three components of stress (σ_θ, σ_x, and σ_r) vary sinusoidally as a function of θ; each component has a similar period, but σ_x has the largest amplitude. Comparing different radial positions, a relatively constant shape is observed for all σ_x plots; the magnitude of this component is highest at the inner wall surface in Fig. 10(*a*) and steadily decreases to the outer radius plotted in Fig. 10(*c*). On the other hand, σ_r and σ_θ both vary significantly in the radial direction peaking at different angles around the tube. Interestingly, the sinusoidal plot representing σ_θ appears to shift through the radial positions: where there is tension at the outer radius, there is compression at the inner radius, and vice versa. All three sinusoidal curves are included in the calculation for σ_{VM}, plotted with a solid line in Fig. 10, resulting in two peaks near the top and bottom of the receiver for all radial positions. It is important to note the stress state described is heavily dependent upon the selected constraints.

The maximum observed von Mises stress during each simulation, $\sigma_{VM,max}$, is plotted as a function of $\Delta T_{w,max}$ for each flux profile at three different pressures in Fig. 11. The values in this plot were calculated assuming a generalized plane strain condition as discussed in Sec. 3. The plotted results indicate that σ_{VM} increases linearly with more aggressive temperature differences across the receiver tube for all pressures; fit parameters for each pressure are detailed in Table 5. Also plotted with a dotted line is the maximum allowable stress for stainless steel 321 at relevant temperatures for melting of solar salt [33]; the temperature where the fitted exponential curve intersects each dotted line is considered the maximum allowable ΔT_w during melting. Values for allowable stress at different temperatures and pressures are tabulated in Table 5. Based on these results with an internal pressure of 1 bar, the maximum ΔT_w should be kept below 78.7 °C and 72.6 °C for heating the receiver wall up to 100 °C and 300 °C, respectively. Based on the results in Figs. 7 and 8, to maintain $\Delta T_w \leq 72.6$°C using only solar flux heating with $\dot{\theta} = 0.5$ deg s^{-1}, the heat input should be $\bar{q} \leq 495$ W m^{-1}, resulting in $t_{melt} \geq 5.6$ h.

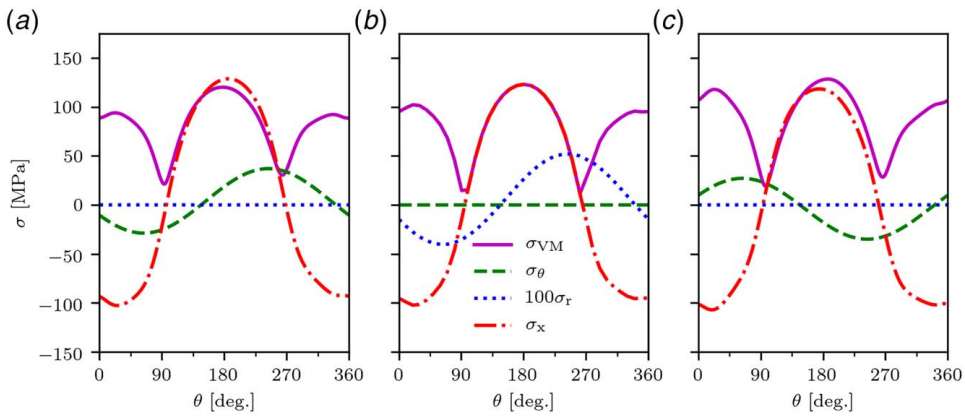

Fig. 10 Circumferential variation of the individual components of thermal stress (σ_θ, σ_r, and σ_x) at p = 1 bar, as well as the von Mises stress, σ_{VM}, plotted at three different radial locations: (*a*) inner radius, (*b*) center of receiver tube, and (*c*) outer radius

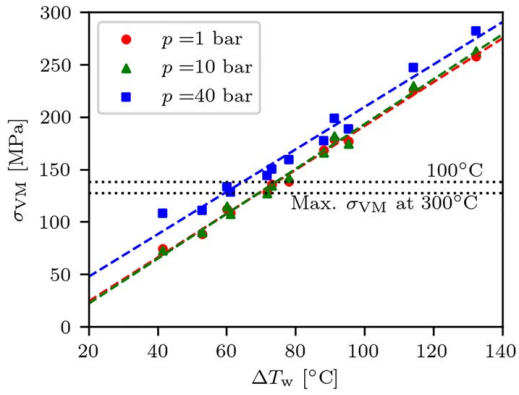

Fig. 11 Maximum von Mises stress as a function of maximum wall temperature difference at various internal tube pressures. The horizontal dotted lines indicate the maximum allowable stress for UNS S32100 at 100 °C and 300 °C [33].

Table 5 Allowable ΔT_w during melting with controllable solar flux heating determined through the thermal stress analysis of CFD results

p (bar)	1		10		40	
$\sigma_{VM}(\Delta T_w)$ fit (MPa)	$2.09\Delta T_w - 17.35$		$2.15\Delta T_w - 22.55$		$2.02\Delta T_w + 8.20$	
R^2	0.993		0.991		0.969	
Average T_w (°C)	100	300	100	300	100	300
Allowable σ_{VM} (MPa)	138	127	138	127	138	127
Allowable ΔT_w (°C)	78.7	72.6	78.9	73.0	65.0	57.6

Note: Results are based on the maximum allowable stress from ASME standards [33].

In this study, no mass flow is assumed so flow pressure is negligible; however, it is interesting to compare the thermal stresses at different internal tube pressures typical during operation. Results shown in Fig. 11 and Table 5 at different pressures suggest that for $P \leq 10$ bar, thermal stresses dominate the stress state and the pressure is of minor importance. In Table 5, the allowable ΔT_w changes by less than 0.5 °C for all cases as the pressure increases from 1 to 10 bar. As the internal pressure continues to increase, the contribution of pressure becomes significant. At $p = 40$ bar, the maximum σ_{VM} observed during melting increased by an average 10.3% compared to 10 bar, resulting in a lower allowable ΔT_w by about 15 °C. The generalized plane strain assumption and 2D formulation provide a conservative estimate of the thermal stresses experienced by the receiver tube, but a three-dimensional (3D) finite-element analysis will be required to accurately capture the constraints of a real system. Such a 3D study is reserved for future work.

The periodic nature of the heat flux profile used to thaw salt frozen in the receiver tube suggests that fatigue is an important mechanism to consider for receiver failure. Figure 12(*a*) shows the transient evolution of the maximum σ_{VM} experienced by the receiver tube during melting with flux profile 10. The cyclical loading during mirror heating has two distinct areas of high loading conditions occurring before and after the onset of melting. As the phase change is initiated, the latent heat component reduces thermal gradients and σ_{VM}, but the stress amplitude during this region remains relatively unchanged. In Fig. 12(*b*), the *x*-axis is adjusted to show more details of the cyclical loading; the time period is selected to include the highest load experienced during melting. When considering the fatigue failure, the total number of cycles is determined by the stress amplitude [34,35]. Referring to Fig. 12(*b*), the stress amplitude for flux profile 10 during the time period of maximum loading is about 49 MPa. This is well below the limit of about 100 MPa for unlimited cycles of stainless steel 321 [33,35]. Idealized fatigue tests generally deal with sinusoidal loading conditions [28], which are not exactly replicated by solar heating as seen in Fig. 12(*b*). However, the low values of stress amplitude suggest that fatigue failure will not be a concern if the $\sigma_{VM,max}$ is maintained below the values indicated in Table 5. Based on these preliminary results, using controllable solar flux heating for freeze recovery will have a minimal impact on the receiver life.

6.5 Hybrid Heating Systems. Results for controllable solar flux heating in the previous sections indicate at least 5.6 h of ideal weather conditions are required to melt salt within the receiver tube while maintaining $\Delta T_w \leq 72.6$ °C. For a more robust freeze recovery process, there could be advantages to a combined

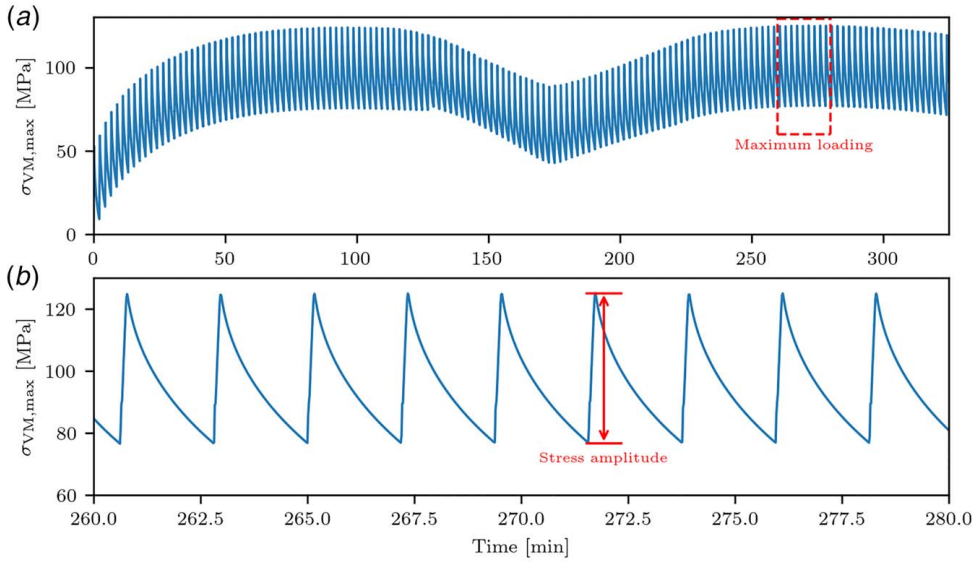

Fig. 12 (*a*) $\sigma_{VM,max}$ in tube during melting from 10 deg to 270 °C with flux profile 10, and (*b*) maximum $\sigma_{VM,max}$ in tube during time of highest load condition illustrating cyclical stress loading and stress amplitude

Table 6 Melting simulation results for mirror heat flux profile 2 augmented with varying levels of impedance heating

Flux profile ID	DNI (W m^{-2})	Impedance heat (W m^{-1})	t_{melt} (min)	$\Delta T_{w,max}$ (K)	% Impedance power
10	1000	0	320.9	72.1	0.0
10	1000	75	281.5	71.2	18.0
10	1000	125	261.0	70.3	26.8

Note: Increasing the impedance power can reduce t_{melt} and, to a lesser extent, $\Delta T_{w,max}$.

mirror/impedance heating method. Such a system would rely on solar heat to provide most of the incident flux, while the added impedance heat prevents cloudy conditions from interrupting the melting process. Coupling with a low-cost impedance heating system (75–125 W m^{-1}) would keep costs manageable compared to pure impedance heating and result in a less weather-dependent system compared to pure solar heating. Results for melting simulation using flux profile 10 with added impedance heating are compared in Table 6.

Results indicate that impedance heating can lower t_{melt}, but has little effect on the wall temperature difference when axial gradients are neglected. With a combined solar and impedance heating system, t_{melt} follows similar trends to those in Fig. 7; however, $\Delta T_{w,max}$ for the combined value of $\bar{q}$ is lower than the pure solar heating results plotted in Fig. 8. With a minimal-cost 75 W m^{-1} impedance system, t_{melt} is reduced by 12.3% from 320.9 to 281.5 min, whereas $\Delta T_{w,max}$ is lowered by 0.9 °C. At this low power level, impedance heat accounts for only 18% of the total energy required to melt the salt, indicating that the hybrid system could still result in significant cost-savings compared to pure impedance heating; 75 W m^{-1} is just enough heat to completely melt the salt, because $q_{melt} = 74.8$ W m^{-1}. However, without additional heat input from the parabolic mirrors, the melting process would take well over a day based on results plotted in Fig. 5.

7 Conclusions

This paper assesses the viability of using controllable solar flux heating for freeze recovery of molten-salt parabolic trough receivers through computational modeling of the melting process. The modeling approach considers a constant density salt with conduction-dominated heat transfer, resulting in conservative melt times. The study shows that the proposed controllable solar flux heating approach has potential to replace or supplement the impedance heating system to reduce the freeze recovery time and reduce the operating costs.

Thermal stresses associated with nonuniform solar flux during the controllable solar flux heating process are also calculated. The analysis indicates that the temperature difference across the receiver wall, ΔT_w, should be maintained below 70 °C for heating up to 300 °C at $p \leq 10$ bar to stay below the maximum allowable stress constraints. At these conditions, the heating process will have a minimal impact on the receiver life. To achieve $\Delta T_w \leq 70$ °C using only solar flux heating with $\dot{\theta} = 0.5$ deg s^{-1}, the selected heat flux profile should have an average heat input of $\bar{q} \leq 495$ W m^{-1}. This value of $\bar{q}$ can be achieved with $t_{on} = 0$ and $t_{off} \geq 117$ s, resulting in a total melting time of $t_{melt} \geq 5.6$ h. Comparing with a total melting time of $t_{melt} = 8.8$ h with a 300 W m^{-1} impedance heating system, the controllable solar flux heating method can be more efficient.

The analysis also shows that a hybrid freeze recovery incorporating both controllable solar flux heating and impedance heating may be advantageous. Both methods can be complementary to each other in practical operation. For a molten-salt plant with a low-cost impedance heating system installed, the mirrors can supplement solar heat to the freeze recovery process to save electrical energy for the impedance heating when solar irradiation is available.

By recognizing the potential of the controllable solar flux heating method, a more comprehensive engineering analysis is required to determine an optimal heating system for molten-salt collector loops in practice. Future modeling efforts will assess the impact of temperature-dependent density and void-space formation on thermal gradients during melting, as well as developing a 3D model to account for axial gradients present in a real system.

Acknowledgment

This work was authored in part by Alliance for Sustainable Energy, LLC, the manager and operator of the National Renewable Energy Laboratory for the U.S. Department of Energy (DOE) under Contract No. DE-AC36-08GO28308. Funding was provided by U.S. Department of Energy Office of Energy Efficiency and Renewable Energy Solar Energy Technologies Office. The views expressed in the article do not necessarily represent the views of the DOE or the U.S. Government. The authors would like to acknowledge Dr. Janna Martinek for many useful conversations regarding model setup and troubleshooting.

References

[1] Price, H., Lüpfert, E., Kearney, D., Zarza, E., Cohen, G., Gee, R., and Mahoney, R., 2002, "Advances in Parabolic Trough Solar Power Technology," ASME J. Sol. Energy Eng., **124**(2), p. 109–125.
[2] Kincaid, N., Mungas, G., Kramer, N., Wagner, M., and Zhu, G., 2018, "An Optical Performance Comparison of Three Concentrating Solar Power Collector Designs in Linear Fresnel, Parabolic Trough, and Central Receiver," Appl. Energy, **231**, pp. 1109–1121.
[3] Chowdhury, M. T., and Mokheimer, E. M. A., 2020, "Recent Developments in Solar and Low-Temperature Heat Sources Assisted Power and Cooling Systems: A Design Perspective," ASME J. Energy Resour. Technol., **142**(4), p. 040801.
[4] NREL, "Concentrating Solar Power Projects," https://solarpaces.nrel.gov/, Accessed February 20, 2019.
[5] Denholm, P., and Hand, M., 2011, "Grid Flexibility and Storage Required to Achieve Very High Penetration of Variable Renewable Electricity," Energy Policy, **39**(3), pp. 1817–1830.
[6] Aqachmar, Z., Allouhi, A., Jamil, A., Gagouch, B., and Kousksou, T., 2019, "Parabolic Trough Solar Thermal Power Plant Noor I in Morocco," Energy, **178**, pp. 572–584.
[7] Peiró, G., Prieto, C., Gasia, J., Jové, A., Miró, L., and Cabeza, L. F., 2018, "Two-Tank Molten Salts Thermal Energy Storage System for Solar Power Plants at Pilot Plant Scale: Lessons Learnt and Recommendations for its Design, Start-up and Operation," Renew. Energy, **121**, pp. 236–248.
[8] Herrmann, U., Kelly, B., and Price, H., 2004, "Two-Tank Molten Salt Storage for Parabolic Trough Solar Power Plants," Energy, **29**(5–6), pp. 883–893.
[9] Liu, M., Steven Tay, N. H., Bell, S., Belusko, M., Jacob, R., Will, G., Saman, W., and Bruno, F., 2016, "Review on Concentrating Solar Power Plants and New Developments in High Temperature Thermal Energy Storage Technologies," Renew. Sustain. Energy Rev., **53**, pp. 1411–1432.
[10] Kelly, B., Price, H., Brosseau, D., and Kearney, D., 2009, "Adopting Nitrate/Nitrite Salt Mixtures as the Heat Transport Fluid in Parabolic Trough Power Plants," Proceedings of ASME Energy Sustainability Conference, Long Beach, CA, 2007.
[11] Vignarooban, K., Xu, X., Arvay, A., Hsu, K., and Kannan, A. M., 2015, "Heat Transfer Fluids for Concentrating Solar Power Systems—A Review," Appl. Ener., **146**, pp. 383–396.
[12] Siegel, N. P., Bradshaw, R. W., Cordaro, J. B., and Kruizenga, A. M., 2011, "Thermophysical Property Measurement of Es2011-540," Proceedings of ASME 5th International Conference on Energy Sustainability, Washington, DC.
[13] Kearney, D., Kelly, B., Herrmann, U., Cable, R., Pacheco, J., Mahoney, R., Price, H., Blake, D., Nava, P., Potrovitza, N., 2004, "Engineering Aspects of a Molten Salt Heat Transfer Fluid in a Trough Solar Field," Energy, **29**(5–6), pp. 861–870.
[14] Gaggioli, W., Fabrizi, F., Rinaldi, L., and Di Ascenzi, P., 2017, "Experimental Tests About the Cooling/Freezing of the Molten Salts in the Receiver Tubes of a Solar Power Plant With Parabolic Trough," AIP Conf. Proc., **1850**(1), p. 020005.
[15] Kolb, G., Ho, C., Iverson, B., Moss, T., and Siegel, N., 2010, "Freeze-Thaw Tests on Trough Receivers Employing a Molten Salt Working Fluid," Proceedings of ASME 4th International Conference on Energy Sustainability, Phoenix, AZ, Vol. 2, pp. 693–698.
[16] Abengoa Solar, LLC,2013, "Development of Molten-Salt Heat Transfer Fluid Technology for Parabolic Trough Solar Power Plant," Public Final Technical Report, DE-FC36-08GO1803.

[17] Kurup, P., and Turchi, C. S., 2015, "Parabolic Trough Collector Cost Update for the System Advisor Model (SAM)", NREL/TP-6A20-65228.
[18] Zalba, B., Marín, J. M., Cabeza, L. F., and Mehling, H., 2003, "Review on Thermal Energy Storage With Phase Change: Materials, Heat Transfer Analysis and Applications," Appl. Therm. Eng., **23**(3), pp. 251–283.
[19] Gomez, J. C., 2011, "Report: High-Temperature Phase Change Materials (PCM) Candidates for Thermal Energy Storage (TES) Applications," Natl. Renew. Energy Lab., **303**, pp. 1–31.
[20] Marugán-Cruz, C., Flores, O., Santana, D., and García-Villalba, M., 2016, "Heat Transfer and Thermal Stresses in a Circular Tube With a Non-Uniform Heat Flux," Int. J. Heat Mass Transf., **96**, pp. 256–266.
[21] Logie, W. R., Pye, J. D., and Coventry, J., 2018, "Thermoelastic Stress in Concentrating Solar Receiver Tubes: A Retrospect on Stress Analysis Methodology, and Comparison of Salt and Sodium," Sol. Energy, **160**, pp. 368–379.
[22] Assis, E., Ziskind, G., and Letan, R., 2009, "Numerical and Experimental Study of Solidification in a Spherical Shell," ASME J. Heat Transfer, **131**(2), p. 024502.
[23] Assis, E., Katsman, L., Ziskind, G., and Letan, R., 2007, "Numerical and Experimental Study of Melting in a Spherical Shell," Int. J. Heat Mass Transf., **50**(9–10), pp. 1790–1804.
[24] Elmozughi, A. F., Solomon, L., Oztekin, A., and Neti, S., 2014, "Encapsulated Phase Change Material for High Temperature Thermal Energy Storage—Heat Transfer Analysis," Int. J. Heat Mass Transf., **78**, pp. 1135–1144.
[25] Burkholder, F., and Kutscher, C. F., 2009, "Heat Loss Testing of Schott's 2008 PTR70 Parabolic Trough Receiver," NREL/TP-550-45633.
[26] ANSYS, 2017, *ANSYS Fluent Theory Guide*, Release 18.2, Help System.
[27] Forristall, R., 2003, "Heat Transfer Analysis and Modeling of a Parabolic Trough Solar Receiver Implemented in Engineering Equation Solver," NREL/TP-550-34169.
[28] Bale, C. W., Bélisle, E., Chartrand, P., Decterov, S. A., Eriksson, G., Gheribi, A. E., Hack, K., Jung, I.-H., Kang, Y.-B., Melançon, J., Pelton, A. D., Petersen, S., Robelin, C., Sangster, J., Spencer, P., and Van Ende, M.-A., 2016, "Reprint of: FactSage Thermochemical Software and Databases, 2010–2016," Calphad, **55**(1), pp. 1–19.
[29] Benages-Vilau, R., Calvet, T., Cuevas-Diarte, M. A., and Oonk, H. A. J., 2015, "The $NaNO_3$–KNO_3 Phase Diagram," Phase Transitions, **89**(1), pp. 1–20.
[30] Zavoico, A. B., 2001, "Solar Power Tower Design Basis Document," SAND2001-2100.
[31] Janz, G. J., Krebs, U., Siegenthaler, H. F., and Tomkins, R. P. T., 1972, "Molten Salts: Volume 3 Nitrates, Nitrites, and Mixtures: Electrical Conductance, Density, Viscosity, and Surface Tension Data," J. Phys. Chem. Ref. Data, **1**(3), pp. 581–746.
[32] Hu, H., and Argyropoulos, S. A., 1996, "Mathematical Modelling of Solidification and Melting: A Review," Model. Simul. Mater. Sci. Eng., **4**(4), pp. 371–396.
[33] ASME, 2017, "Boiler and Pressure Vessel Code, Section II, Part D (Metric)," BPVC.II.D.M-2017.
[34] Lalanne, C., 2014, *Fatigue Damage*, 3rd ed., Vol. 4, Wiley, Hoboken, NJ.
[35] Prasad Reddy, G. V., Dinesh, P. M., Sandhya, R., Laha, K., and Jayakumar, T., 2016, "Behavior of 321 Stainless Steel Under Engineering Stress and Strain Controlled Fatigue," Int. J. Fatigue, **92**(1), pp. 272–280.
[36] Turchi, C. S., Stekli, J., and Bueno, P. C., 2018, *Chapter 11: Concentrating Solar Power*, United States, pp. 373–402.
[37] Pfleger, N., Bauer, T., Martin, C., Eck, M., and Wörner, A., 2015, "Thermal Energy Storage—Overview and Specific Insight Into Nitrate Salts for Sensible and Latent Heat Storage," Beilstein J. Nanotechnol., **6**(1), pp. 1487–1497.
[38] AzoMaterials, "Stainless Steel—Grade 321 (UNS S32100)", https://www.azom.com/article.aspx?ArticleID=967, Accessed October 23, 2001.